Journal of High Energy Astrophysics 23 (2019) 23–28

Contents lists available at ScienceDirect

Journal of High Energy Astrophysics

www.elsevier.com/locate/jheap

Studies on the time response distribution of *Insight*-HXMT/LE

Xiao-Fan Zhao [a,b], Yu-Xuan Zhu [a,c], Da-Wei Han [a], Wei-Wei Cui [a], Wei Li [a], Juan Wang [a], Yu-Sa Wang [a], Yi Zhang [a], Yan-Ji Yang [a], Bo Lu [a], Jia Huo [a], Zi-Liang Zhang [a], Tian-Xiang Chen [a], Mao-Shun Li [a], Zhong-Hua Lv [a,b], Yong Chen [a,*]

[a] Institute of High Energy Physics, Chinese Academy of Sciences, Beijing 100049, China
[b] University of Chinese Academy of Sciences, Beijing 100049, China
[c] College of Physics, Jilin University, Changchun 130012, China

ARTICLE INFO

Article history:
Received 26 June 2019
Received in revised form 15 August 2019
Accepted 26 August 2019

Keywords:
Time response distribution
Long exposure readout mode
Swept charge device
CCD236

ABSTRACT

The Hard X-ray Modulation Telescope (HXMT) named *Insight* is China's first X-ray astronomical satellite, with the Low Energy X-ray Telescope (LE) as one of its main payloads onboard. The detectors of LE adopt swept charge device CCD236 using L-shaped transfer electrodes. To measure the time response distribution resulted from the continuous readout of charges in detection area along specific paths, a long exposure readout mode has been designed. In this mode, CCD236 firstly performs exposure without readout, then all charges generated in preceding exposure phase are read out completely. And an analysis of the photons readout time in this mode is carried out, to obtain the time response distribution.

1. Introduction

As China's first X-ray astronomical satellite, The Hard X-ray Modulation Telescope (Li and Wu, 2008) was launched on June 15, 2017 and named as *Insight*. The concept of *Insight* was originally proposed in the 1990s, which is based on the Direct Demodulation Method (Li and Wu, 1993, 1994). *Insight* carries three main payloads: High Energy X-ray Telescope (HE), Medium Energy X-ray Telescope (ME) and Low Energy X-ray Telescope (LE). Among them, LE covers the energy band of 0.7–13 keV and uses detector arrays and collimators to collect X-ray photons (Chen et al., 2018; Zhang et al., 2014). The swept charge device CCD236 is adopted as detector because of its high energy resolution and high time resolution. The CCD236 is based on charge coupled device (CCD) technology, and is electrically configured similar to a linear CCD (Holland and Pool, 2008). Charges generated in detection area are swept to the central readout amplifier continuously along specific paths, so the position information of charges cannot be given (Smith et al., 2015). Readout time of charges generated in different detection area are constant and related to the positions of charges, which leads to a photon arrival time delay distribution — time response distribution (TRD), making the measurement of TRD critical due to its impact on the photon arrival time recorded by detector.

Pulse profiles observed on the isolated pulsars are employed by LE to calibrate its timing system (Zhang et al., 2018). Pulse profiles accompanied with the corresponding phase-resolved spectra help explore pulsar radiation model. Similar to the photon arrival time, TRD also affects pulse profile through changing the shape and causing a phase delay (Ge, 2012). Thus it is necessary to restore the pulse profile by TRD. In addition, TRD is a significant part of getting time resolution of LE.

Long exposure readout mode (LERM) as a special readout mode of LE, can be used on the measurement of TRD. Differing from normal readout mode (NRM), the readout of charges in detection area is not continuous. CCD236 firstly performs exposure without readout for a specific period, then all charges generated in the preceding exposure phase are read out completely. This paper is focused on the measurement of TRD in LERM. The following section introduces the readout method of CCD236 and the influences of collimators. In Section 3, we describe LERM in detail. Data analysis comes in Section 4. In next section, we discuss the results, followed by the conclusion drawn from all above analysis in the last section.

2. Low energy X-ray telescope

2.1. Readout method of CCD236

CCD236 is the second generation of swept charge device developed for X-ray spectroscopy. It is designed for LE, and used in

* Corresponding author.
E-mail addresses: zhaoxf@ihep.ac.cn (X.-F. Zhao), zhuyx@ihep.ac.cn (Y.-X. Zhu), ychen@ihep.ac.cn (Y. Chen).

https://doi.org/10.1016/j.jheap.2019.08.002
2214-4048/

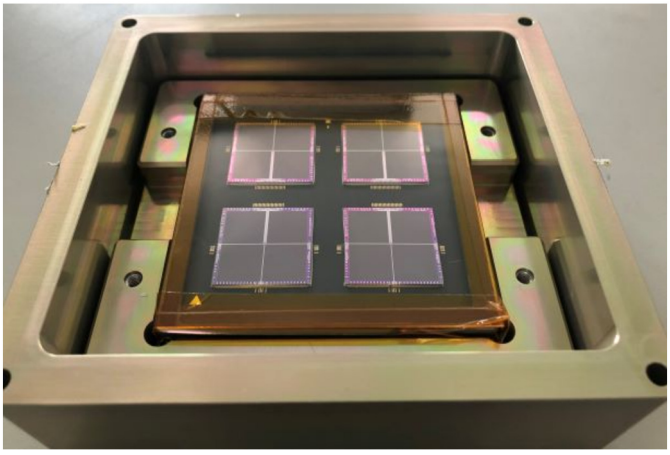

Fig. 1. CCD236 is divided into four quadrants and four CCD236 detectors are packaged on an aluminum nitride ceramic substrate to make up a detector module.

India's Chandrayaan-2 Large Soft X-ray Spectrometer instrument as well (Radhakrishna et al., 2011; Smith et al., 2012). Comparing to the first generation swept charge device, CCD236 benefits a lot from its significant improvements, such as a large detection area over 4 cm^2, the reduction of the drive phases from three to two so as to simplify the clocking (Holland and Pool, 2008), the increase of element pitch from 0.02 mm to 0.1 mm for reducing charge transfer times and an improvement in radiation hardness (Gow et al., 2009, 2015).

CCD236 is divided into four quadrants, and locates its output at central region. In order to realize large-area detector arrays, four CCD236 detectors are packaged on an aluminum nitride ceramic substrate to make up a detector module. Fig. 1 shows the detector module with four CCD236 detectors.

To enable the suppression of surface dark current, CCD236 is clocked continuously, so the position information of charge signals cannot be given (Smith et al., 2013). Because of its L-shaped transfer electrodes, charges generated in detection area are firstly transferred to diagonal of CCD236 along the direction perpendicular to transfer electrodes and then to the central output along the diagonal. The transfer time for charges generated in one L-shaped detection area are the same. We call pixels in one L-shaped detection area as a "packed-pixel" and there are 100 packed-pixels per quadrant. In addition, there are 20 pixels from central output to the L-shaped detection area. For convenience, we also call these 20 pixels as packed-pixels, so there are a total of 120 packed-pixels from central output to the edge of CCD236 in each quadrant. Fig. 2 displays schematic representation of electron flow transfer paths.

Among 120 packed-pixels, the area of about 20 packed-pixels near central output is considerately small, comparing to the gradually increasing area for the subsequent 98 packed-pixels. Due to the large noise, charges generated in the outermost 2 packed-pixels near the edge of CCD236 are exported outside detector directly, instead of getting involved in readout system. In other words, the outermost 2 packed-pixels are designed as invalid pixels.

With the working frequency of 100 kHz, all charges would be readout within 1.18 ms. Continuous readout which mixes the charges from different packed-pixels, makes it impossible for us to tell the location and time of charges generation. However, we could obtain the probability of different readout time statistically through TRD.

2.2. The collimators and field of views

LE combines a variety of field of views (FOVs) to accomplish scientific observation. There is a collimator on top of each detector module to limit both narrow FOV ($1.6° \times 6°$) and wide FOV ($4° \times 6°$). Besides these two FOVs, blocked FOV is added for the sake of better deducting background in both pointing observation and all-sky survey observation, but with no capability to collect X-ray photons from target source. This paper will not further discuss about blocked FOV. The three kinds of FOVs are limited by long collimator. In addition, LE also designs a short collimator in order to monitor large-area sky in scanning observation, which brings an all-sky monitoring (ASM) FOV. The ASM FOV is a trapezoidal FOV. The birds-eye schematic of two kinds of collimators are shown in Fig. 3.

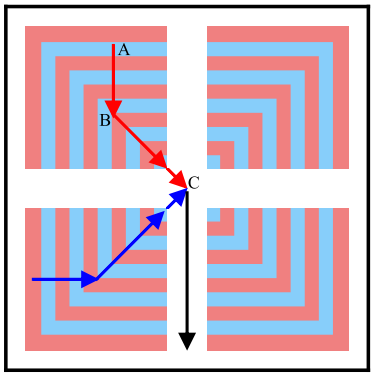

Fig. 2. Schematic of electron flow transfer paths. Charge generated in position A is firstly transferred to position B along the direction perpendicular to the electrodes. Then it is transferred to the output C along diagonal. We call pixels in one L-shaped detection area as a "packed-pixel". The time needed for the readout of charges in one packed-pixel are the same. The transfer paths of charges generated in other quadrants of CCD236 are similar, which is shown with blue lines. (For interpretation of the colors in the figure(s), the reader is referred to the web version of this article.)

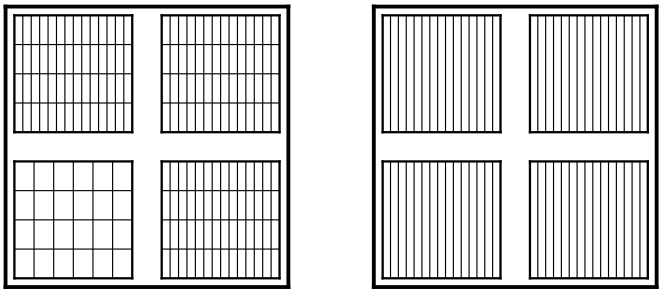

Fig. 3. The birds-eye schematic of long collimator with 3 narrow FOVs and a wide FOV (left), and the birds-eye schematic of short collimator with 4 ASM FOVs (right).

When observing an X-ray source, the collimator has an occlusion effect on CCD236, especially for those pixels under collimators. Given the differences between TRD caused by the structures of all kinds of collimators, it is necessary to treat different FOVs, respectively.

3. Long exposure readout mode

In order to get the position information of charge signals, Smith et al. (2013) has made several useful attempts. One idea is to place an organic light emitting diode (OLED), which has a slightly larger area than CCD236, in proximity with the CCD236 to provide a position-dependent signal. The other is to use X-ray beamline with 3 mm spot size for scanning the CCD236 horizontally and vertically, thus providing a position-dependent signal which can be recorded to obtain the response of CCD236 at different position. Limited by the inability to get the pinpoint of single pixel, the results are not proven. Therefore, instead of obtaining the time

response of each single pixel, LE designs long exposure readout mode to get TRD statistically.

There are two readout modes designed for LE: NRM and LERM. NRM is the default readout mode, in which charges are transferred to output continuously without position information. If the signal amplitude is higher than threshold, an over threshold trigger would be recorded with its energy, arrival time and detector ID, which is called a "physical event". In addition, in order to monitor the signal baseline level of each detector, the LE forcibly collects amplitude of each detector every 32 ms in turn, which is called a "forced trigger event". LE box possesses 4 readout modules for 32 detectors in total, and every 8 detectors share the same readout module. Forced trigger events have a higher priority than physical events. When the forced trigger events are being recorded, other events could not be read out for all detectors in the same readout module. As a result, there are a portion of physical events that cannot be read out.

In LERM, charges are not transferred continuously. CCD236 firstly performs exposure for a certain duration from several ms to several hundred ms, during which the driving clock is paused, and charges are stored in CCD236. In the meantime, forced trigger events are not recorded either. Later, all charges in the chip will be continuously transferred and read out. We design 150 clock cycles so that all charges generated in preceding exposure phase should be read out completely, during which the readout of forced trigger events is resumed.

In continuous readout phase of LERM, charges stored in different packed-pixels are read out in sequence. The one closest to output is read out firstly. After 118 clock cycles, all charges in the chip are read out. Nevertheless, new charges will generate during continuous readout phase, in consideration of the existence of incident X-ray photons meantime. These photons are assumed as out-of-time photons in LERM.

The main work frequency of LE is 100 kHz. Based on this work frequency, LE designs 7 kinds of exposure time, which are 2 ms, 5 ms, 10 ms, 20 ms, 50 ms, 100 ms and 200 ms. As the exposure time increases, the dark current of CCD236 increases. This paper utilizes the first 5 exposure time to measure time response distribution.

4. Data analysis

4.1. Data set

In ground experiments, we thoroughly test the long exposure readout mode of 5 kinds of exposure time in a vacuum chamber. X-ray is generated mainly through fluorescence of vacuum chamber interior wall that is stimulated by the bremsstrahlung radiation from an X-ray tube, hence the X-ray source is recognized as a diffused source.

During the period of in-orbit operation, LE is applied to observe the source Swift J0243.6+6124 in 10 ms long exposure readout mode. Swift J0243.6+6124 is a Galactic ultraluminous X-ray pulsar discovered by *Swift* with a rotation period measured as 9.86 s (Kennea et al., 2017; Jenke and Wilson-Hodge, 2017).

4.2. Split events reconstruction

The split events are generated when an X-ray photon interacts with two or more adjacent pixels. The criterion of split events for LE in NRM is that the arrival time interval of two or more events is equal to or less than clock cycle (0.01 ms for 100 kHz working frequency). In LERM, charges are stored in pixels before readout, and two or more neighboring single events may mistakenly be recognized as split events. In this paper, we analyze the effect of split events reconstruction according to the experimental results.

4.3. Epoch folding

In order to obtain the X-ray photon counts of each clock cycle in readout phase, an epoch folding has been conducted. The actual period of LERM has deviation from expectation. For example, the whole period of 10 ms long exposure is supposed to be 11.5 ms (10 ms exposure time and 1.5 ms readout time). Nevertheless, actual period is about 11.4992 – 11.4997 ms and is time-dependent. Charges in pixels are driven by the clock of LE box, but their arrival time information of events is provided by the clock of satellite platform. Therefore, two clocks cannot be completely consistent due to temperature drift. After epoch folding, the TRD would have a large deviation from actual TRD.

In consideration of the periodicity of forced trigger events driven by the clock of LE box, we recognize arrival time of forced trigger events as a time ruler to scale arrival time of physical events, through which we solved the problem of clock inconsistency.

4.4. Correction for forced trigger events

After epoch folding, we obtain the X-ray photon counts of each clock cycle in readout phase, and find out 3 unusually low counts due to the readout of forced trigger events. In LERM, forced trigger events only appear in 3 fixed clock cycles and they have higher priority than physical events. There is a certain proportion of time that physical events cannot be readout in these 3 specific clock cycles. In the readout time of 150 clock cycles, an average of 0.5 forced trigger events will appear in each of these 3 positions. When reading out forced trigger events, a total of 8 detectors cannot be read out, accounting for a quarter of all detectors, as a result of which LE cannot read out physical events for one eighth of time. Fig. 4 shows the correction for forced trigger events.

4.5. Correction for out-of-time events

In LERM, the charges generated in exposure phase are of great significance to us. However, in the following readout phase there are still charges generated in pixels, which are recognized as out-of-time events. Charges in exposure phase are read out successively in first 118 clock cycles and those in readout phase are read out equiprobably in 150 clock cycles. We use the average photon counts collected in the last 32 clock cycles as out-of-time photon counts. After subtracting the out-of-time events, we finally obtain TRD.

From the result we could know that the counts of first 16 packed-pixels near output are so small that they can be ignored. The counts of subsequent 102 packed-pixels increase gradually in a roughly linear pattern, which is in agreement with the detection area of each packed-pixel in CCD236. In the trend of linear growth, there are several concave structures caused by collimators. Next section will describe the reason in detail. The last packed-pixel is affected by outermost invalid packed-pixels, so its noise is relatively large.

5. Results

5.1. Comparison for split events reconstruction

We compulsorily perform a split events reconstruction by the criterion of NRM. Results are shown in Fig. 5. Raw events, single events, reconstruction events stand for all events without reconstruction, single events during split events reconstruction and the sum of single events and split events, respectively. The TRD for raw events, single events and reconstruction events are almost identical except the outermost packed-pixels shown in Fig. 5. In the last

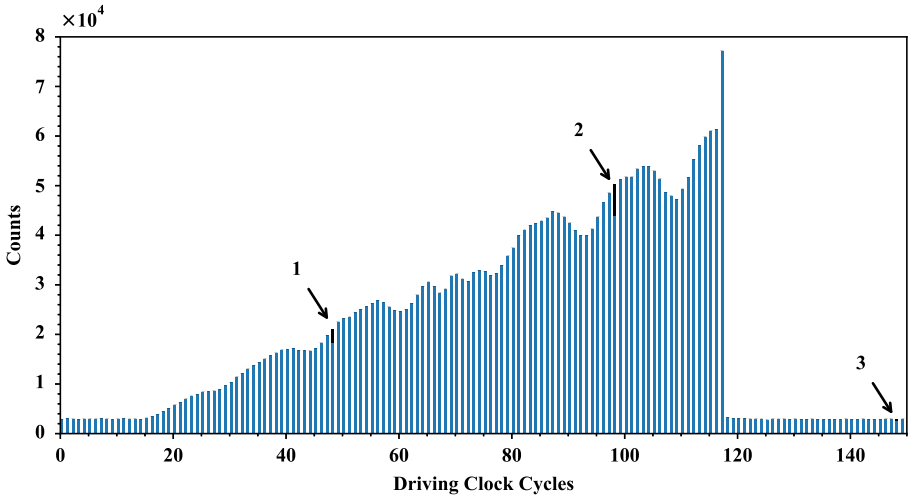

Fig. 4. X-ray photon counts of each driving clock cycle for narrow FOV in 10 ms LERM. We take the result of narrow FOV in 10 ms LERM as an example. The results of other FOV and other exposure time are similar. There are 3 positions where the counts are unusually lower than surrounding counts. The intervals between 3 positions are 50 clock cycles. These three black bars stand for event counts that are not read out because of forced trigger events.

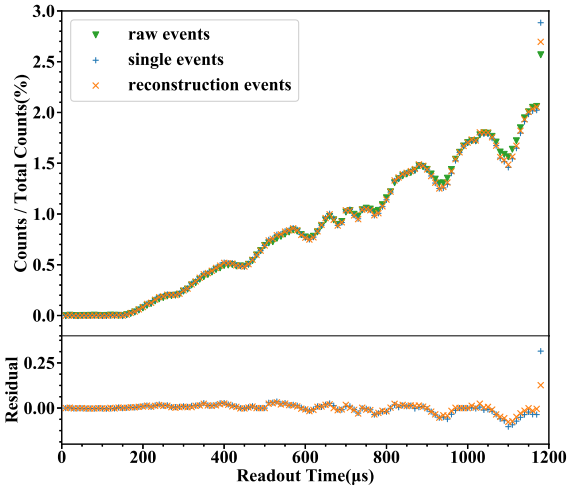

Fig. 5. TRD for narrow FOV in 10 ms LERM. The statistical error is small, so we didn't draw it. Instead, we plot residual based on raw events. The X axis is transformed to readout time through driving clock cycle. The results of other FOV and other exposure time are similar.

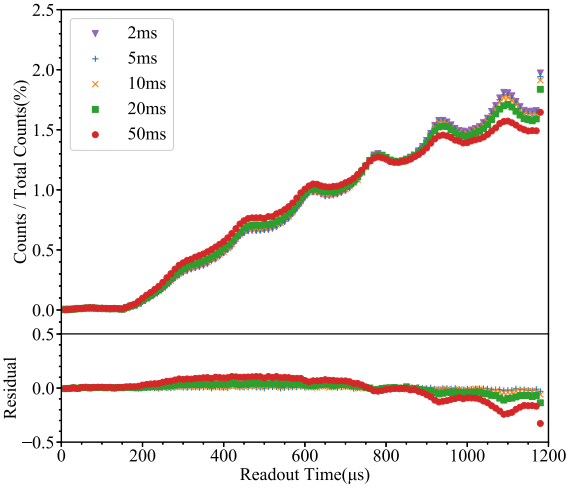

Fig. 6. TRD for ASM FOV in 5 kinds of exposure time. Residual is based on 2 ms LERM. The results of other FOV are similar.

packed-pixel, the ratio is the biggest for single events, while the smallest for raw events.

When X-ray photons generate split events in the 118th and 119th packed-pixels, charges in the 118th packed-pixel are recorded and those in 119th packed-pixel are discarded because of its unavailability. After split events reconstruction, charges in the 118th packed-pixel are mistakenly recognized as single events, which leads to the increment of ratio in single events. In consideration that the difference is less than 0.5%, this paper adopts the results without split events reconstruction.

5.2. Long exposure time

During the period of in-orbit operation, only 10 mm exposure time has been employed to observe, so the ground experiments is a better way to illustrate the effect of exposure time. In ground experiments we tested 5 kinds of exposure time in LERM. The results of ASM FOV are shown in Fig. 6. As exposure time gradually increases, the count ratios of packed-pixels with smaller detection area also gradually increase, and those with larger detection area gradually decrease.

Table 1
Counting rate of out-of-time events and long exposure events for ASM FOV in 5 kinds of LERM.

No.	Exposure time	Counting rate of out-of-time events	Counting rate of long exposure events
1	2 ms	289.7 ± 0.3 counts s^{-1}	283.5 ± 0.1 counts s^{-1}
2	5 ms	290.6 ± 0.4 counts s^{-1}	276.9 ± 0.1 counts s^{-1}
3	10 ms	290.2 ± 0.7 counts s^{-1}	266.0 ± 0.2 counts s^{-1}
4	20 ms	289.3 ± 0.7 counts s^{-1}	246.4 ± 0.1 counts s^{-1}
5	50 ms	289.2 ± 1.1 counts s^{-1}	197.8 ± 0.1 counts s^{-1}

The pileup effect of LE is small in NRM, while it is significantly higher in LERM. Due to the continuous readout, the counting rate of out-of-time events can be concluded as the actual counting rate of X-ray photons. Except for events mentioned above, the rest of events are all summed as long exposure events. Table 1 lists the counting rate of out-of-time events and long exposure events in ASM FOV for 5 kinds of exposure time.

The X-ray intensities indicated by the counting rate of out-of-time events are the same in 5 kinds of long exposure experiments. As the exposure time increases, the counting rate of long exposure events continues to decrease, suggesting an increasing pileup ef-

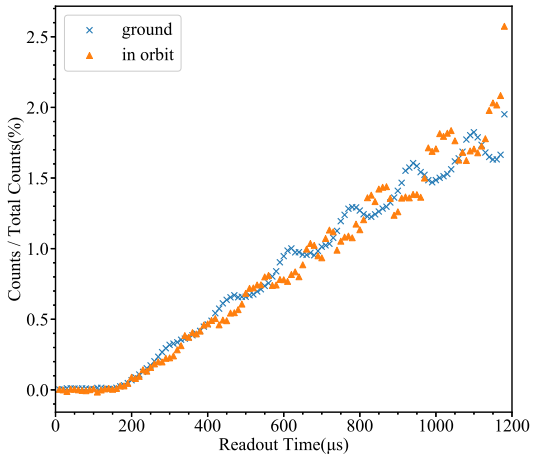

Fig. 7. TRD for 10 ms ASM FOV in ground and in-orbit experiments.

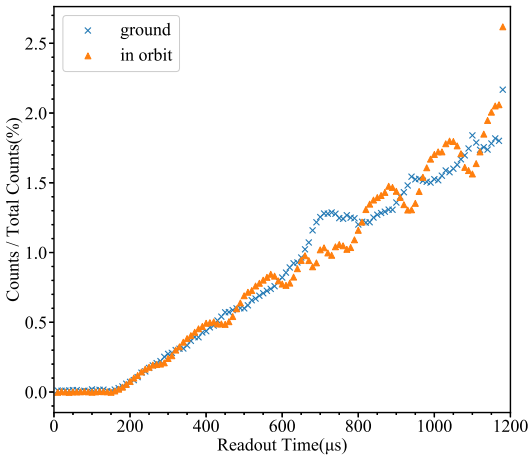

Fig. 9. TRD for 10 ms narrow FOV in ground and in-orbit experiments.

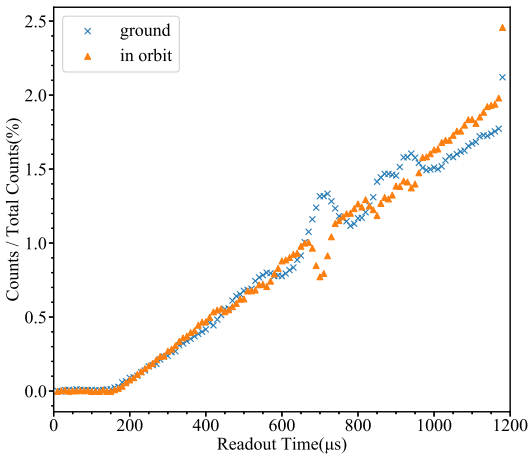

Fig. 8. TRD for 10 ms wide FOV in ground and in-orbit experiments.

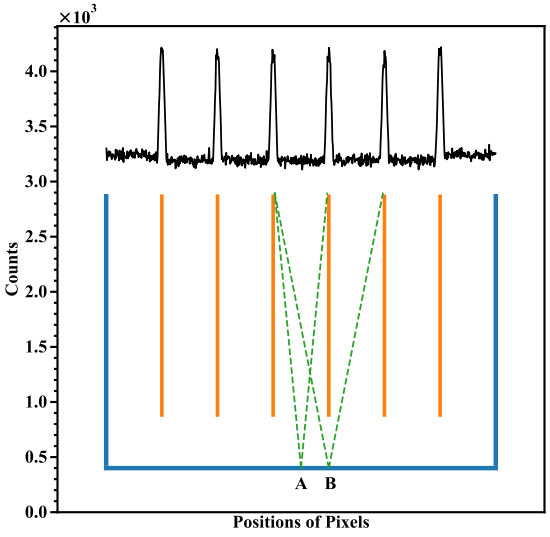

Fig. 10. The photon counts distribution under the illumination of a diffused source from simulation results (black line). The yellow lines represents the collimators. Under the illumination of a diffused source, the photon counts from pixels under collimators (point B) is larger than those not under collimators (point A).

fect. As a result, the ratios of packed-pixels with larger detection area become smaller.

5.3. The influence of FOV

TRDs for ASM FOV, wide FOV and narrow FOV in ground and in-orbit experiments are respectively shown in Fig. 7, Fig. 8 and Fig. 9. In ground experiments there are several convex structures. On the contrary, there are several concave structures in orbit.

ASM FOV, wide FOV and narrow FOV have 3 kinds of collimators shown in Fig. 3. The collimators whose positions correspond with the convex and concave structures in TRD block X-ray photons and lead to special convex and concave structures in TRD.

Ground observation and in-orbit observation present diametrically opposite results. In ground experiments, the source is fluorescence of vacuum chamber interior which is recognized as a diffuse source, and the angle of view from pixels under collimators is larger than that not under collimators. We use a simplified one-dimensional model to simulate the effects of the collimators whose result is displayed in Fig. 10. Under the illumination of a diffused source, the photon counts from pixels under collimators is larger than those not under collimators. In contrast, the X-ray from Swift J0243.6+6124 in orbit is recognized as collimated X-ray. The blocking of collimator should form a concave structure.

6. Conclusions

CCD236 is the second generation swept charge device with L-shaped transfer electrodes and continuous readout, which leads to a TRD for photons arrival time. We design a long exposure readout mode to measure TRD in ground and in-orbit experiments.

The whole tendency of time response distribution is similar for both ground and in-orbit experiments. With the working frequency of 100 kHz, all charges would be read out within 1.18 ms. The event counts read out in first 16 driving clock cycles are so small that they can be neglected. And event counts in each driving clock cycle increase rough linearly for the following 102 driving clock cycles except several convex structures in ground experiments and concave structures in orbit. The differences are caused by the blocking of collimators when observing diffused and collimated X-ray sources. With the increment of pileup effect, count ratios for packed-pixels with smaller detection area increase and those with larger detection area decrease.

Acknowledgments

This work made use of the data from the HXMT mission, a project funded by China National Space Administration (CNSA) and

the Chinese Academy of Sciences (CAS). We are very grateful to Shu Zhang, Ming-Yu Ge and You-Li Tuo for their constructive comments and suggestions.

References

Chen, Y., Cui, W.-W., Li, W., Wang, J., Han, D.-W., Wang, Y.-S., Chen, T.-X., Zhang, Y., Yang, Y.-J., et al., 2018. Spacecr. Eng. 27, 134.
Ge, M.-Y., 2012. The X-Ray Emission of Pulsars. PhD thesis, Institute of High Energy Physics Chinese Academy of Sciences.
Gow, J., Holland, A.D., Pool, P., 2009. In: Proc. SPIE 7435, UV, X-Ray, and Gamma-Ray Space Instrumentation for Astronomy XVI, vol. 74350.
Gow, J.P.D., Smith, P.H., Pool, P., Hall, D.J., Holland, A.D., Murray, N.J., 2015. J. Instrum. 10, C01037.
Holland, A., Pool, P., 2008. In: Proc. SPIE 7021, High Energy, Optical, and Infrared Detectors for Astronomy III, vol. 702117.
Jenke, P., Wilson-Hodge, C.A., 2017. The Astronomer's Telegram. 10812.
Kennea, J.A., Lien, A.Y., Krimm, H.A., Cenko, S.B., Siegel, M.H., 2017. The Astronomer's Telegram. 10809.
Li, T.-P., Wu, M., 1993. Astrophys. Space Sci. 206, 91.
Li, T.-P., Wu, M., 1994. Astrophys. Space Sci. 215, 213.
Li, T.-P., Wu, M., 2008. Physics 37, 648.
Radhakrishna, V., Narendranath, S., Tyagi, A., Bug, M., Unnikrishnan, U., Kulkarni, R., Sreekantha, C.V., Kumar, et al., 2011. In: Lunar and Planetary Science Conference. 42, p. 1708.
Smith, P.H., Gow, J.P.D., Murray, N.J., Holland, A.D., Anand, M., Pool, P., Sreekumar, P., Narendranath, S., 2012. In: Proc. SPIE 8453, High Energy, Optical, and Infrared Detectors for Astronomy, vol. 84530R.
Smith, P.H., Gow, J.P.D., Pool, P., Holland, A.D., 2015. J. Instrum. 10, C03041.
Smith, P.H., Murray, N.J., MacCormick, C., Gow, J.P.D., Weatherill, D., Allanwood, E., Pool, P., Holland, A.D., 2013. In: Proc. SPIE 8859, UV, X-Ray, and Gamma-Ray Space Instrumentation for Astronomy XVIII, vol. 88590M.
Zhang, S., Lu, F.-J., Zhang, S.-N., Li, T.-P., 2014. In: Proc. SPIE 9144, Space Telescopes and Instrumentation 2014: Ultraviolet to Gamma Ray, vol. 914421.
Zhang, S., Zhang, S.-N., Lu, F.-J., Li, T.-P., Song, L.-M., Xu, Y.-P., Wang, H.-Y., Qu, J.-L., et al., 2018. In: Proc. SPIE 10699, Space Telescopes and Instrumentation 2018: Ultraviolet to Gamma Ray, vol. 106991U.